Neural Architectures of Slow and Fast Dynamics in the Human Brain

Yuhan Lu[1,2,3,†], Zhuoran Li[4,†], Hangze Mao[5,†], Qinsiyuan Lyu[2,3], Chen Yao[6], Junxi Chen[7], Louis Tao[4,8], Zhuo-Cheng Xiao[1,3,9*], Xing Tian[1,3,*]

[1]Division of Arts and Sciences, New York University Shanghai, Shanghai 200122, China

[2]Shanghai Key Laboratory of Brain Functional Genomics (Ministry of Education), School of Psychology and Cognitive Science, East China Normal University, Shanghai 200062, China

[3]NYU-ECNU Institute of Brain and Cognitive Science, New York University Shanghai, Shanghai 200062, China

[4]Center for Quantitative Biology, Academy for Advanced Interdisciplinary Studies, Peking University, Beijing, 100871, China

[5]School of Medical Technology and Information Engineering, Zhejiang Chinese Medical University, Hangzhou, 310053, China

[6]Department of Neurosurgery, Shenzhen Second People's Hospital, Shenzhen 518035, China.

[7]Department of Neurosurgery, Guangzhou Sanjiu Brain Hospital, Guanzhou 510510, China

[8]Center for Bioinformatics, National Laboratory of Protein Engineering and Plant Genetic Engineering, School of Life Sciences, Peking University, Beijing 100871, China

[9]NYU-ECNU Institute of Mathematical Sciences, New York University Shanghai, Shanghai 200062, China

[†]These authors have contributed equally to this work.

***Corresponding author:**

Xing Tian, E-mail: xing.tian@nyu.edu

Zhuo-Cheng Xiao, E-mail: xiao.zc@nyu.edu

Abstract

The human brain navigates a vast temporal landscape, bridging rapid millisecond dynamics of perception and action to the slow patterns of internal physiological regulation. This multi-scale capacity is traditionally attributed to a unitary, hierarchical gradient of intrinsic timescales. However, this unidimensional model fails to explain how local circuits can simultaneously sustain rapid behavioral responses and slow, body-coupled dynamics. Here, we resolve this fundamental tension by demonstrating that the human brain is organized into two parallel and functionally dissociable temporal architectures. Using a novel method, SPLIT (spectral piecewise-linear inference of timescales), applied to large-scale stereo-electroencephalography (8,619 contacts from 185 individuals), we dissociate fast (~10-100 Hz) and slow (~1-10 Hz) temporal components. We show that the fast-component timescales exclusively organize into the canonical sensory-to-transmodal hierarchy and capture fine-grained anterior-posterior gradients within the hippocampus and insula. In contrast, the slow-component timescales lack hierarchical structure and are selectively coupled to cardiac-related physiological signals. This dual architecture persists across wakefulness, resting state, sleep, and anesthesia, suggesting an intrinsic organizational principle. Our findings overturn the unitary view of brain timescales, establishing a bipartite framework where parallel temporal components simultaneously orchestrate perception, cognition, and action while maintaining neurovisceral regulation.

Main

To survive and flourish, the human brain must rapidly interact with the environment while maintaining stable internal physiology. It must therefore support computations across orders of magnitude in time, ranging from rapid sensory processing and action to slow cognitive integration and allostatic regulation[1-5]. A prevailing view holds that this multiscale capacity is unidimensionally embedded in a cortical hierarchy, characterized by a monotonic increase of the intrinsic neural timescale from sensory to transmodal regions[6-12] (i.e., the gradient of timescales). However, this hierarchy-spanning network architecture is also implicated in much slower interoceptive monitoring and visceromotor control of peripheral physiology[13,14]. This raises a key organizational question: does each region operate around a single dominant intrinsic timescale, such that the cortex is described by one unidimensional gradient, or do local circuits contain separable temporal components that map onto multiple, parallel gradients serving distinct functional demands (**Fig. 1a**)? Investigating the organizing principle would provide a holistic picture of the brain's temporal architecture, the scaffold on which neural computations unfold[8,15,16] and whose alteration drives transitions from healthy cognition to neuropsychiatric disorders[17,18].

Addressing this organizational question requires revisiting a tacit assumption that has guided most work on the brain-wide temporal hierarchy: a region's activity can be approximated by a single dominant timescale. Accordingly, widely-used methods, such as autocorrelation decay[9,10,19-24] or spectral knee frequency[25-29], reduce an aggregated time series (e.g., local field potentials [LFPs] or BOLD signals) to a single timescale per region, and the "the gradient of timescale" is inferred by comparing these regional scalars across cortex[10,25,30]. However, multiple timescales can co-exist within the same local circuits[28,29,31,32], making single-timescale reduction oversimplified and potentially biased because it conflates distinct temporal components, and therefore challenging the unidimensional view of the brain's temporal architecture.

Resolving the debate about organizing principle of brain-wide temporal infrastructure require brain-wide recordings with millisecond temporal precision and broad anatomical coverages [3,9,32], which is an uncommon combination in human neuroscience. Large-scale stereo-electroencephalography (sEEG) bridges this gap by sampling mesoscopic population dynamics at high rates across cortex and deep structures, providing a natural substrate for linking microcircuit timescale diversity to brain-wide organization. We therefore approach the question as component-resolved inference: by identifying timescales within LFPs without a single-timescale prior, we examine brain-wide distribution of timescales and examine whether the human brain's temporal infrastructure follows a unidimensional gradient or dissociable architectures.

Applying SPLIT (spectral piecewise-linear inference of timescales) algorithm for robust estimation of timescales to a large-scale human sEEG recordings (total of 8,619 contacts from 185 subjects), we revealed a brain-wide organization of dissociable fast (~10-100 Hz) and slow (~1-10 Hz) components of timescales. Only the fast component recapitulated the canonical cortical and local-regional hierarchy, whereas the slow component ubiquitously

related to physiological measures, such as cardiac rhythms. The two-track brain-wide temporal infrastructure was stable across different conscious states, demonstrating the inherent nature of the neural architecture. We suggest multiple, parallel temporal computations of the human brain for collectively regulating the body and interacting with the environment.

Simulations depict the relations between dynamics of single and multiple timescales

To establish a theoretical foundation for resolving whether LFP dynamics could exhibit single or multiple timescales, we first interrogated how the integration of microcircuit activity manifested in mesoscopic field potentials. We used Ornstein-Uhlenbeck (OU) simulations with controlled latent time constants and coupling. These simulations showed that when the number of timescales expressed in the observable was not fixed, a linear mixture of uncoupled components could yield multiple knees (equivalent to timescale τ expressed the time domain, i.e., $\tau \propto 1$ / freq_knee) in LFP spectrum, whereas the coupling collapsed dynamics into eigenmodes and produced one or multiple dominant knees depending on interaction strength and structure (**Fig. 1b**, also see **Fig. S1**). Thus, the number of LFP timescales was an emergent property jointly determined by the latent timescales and their interactions.

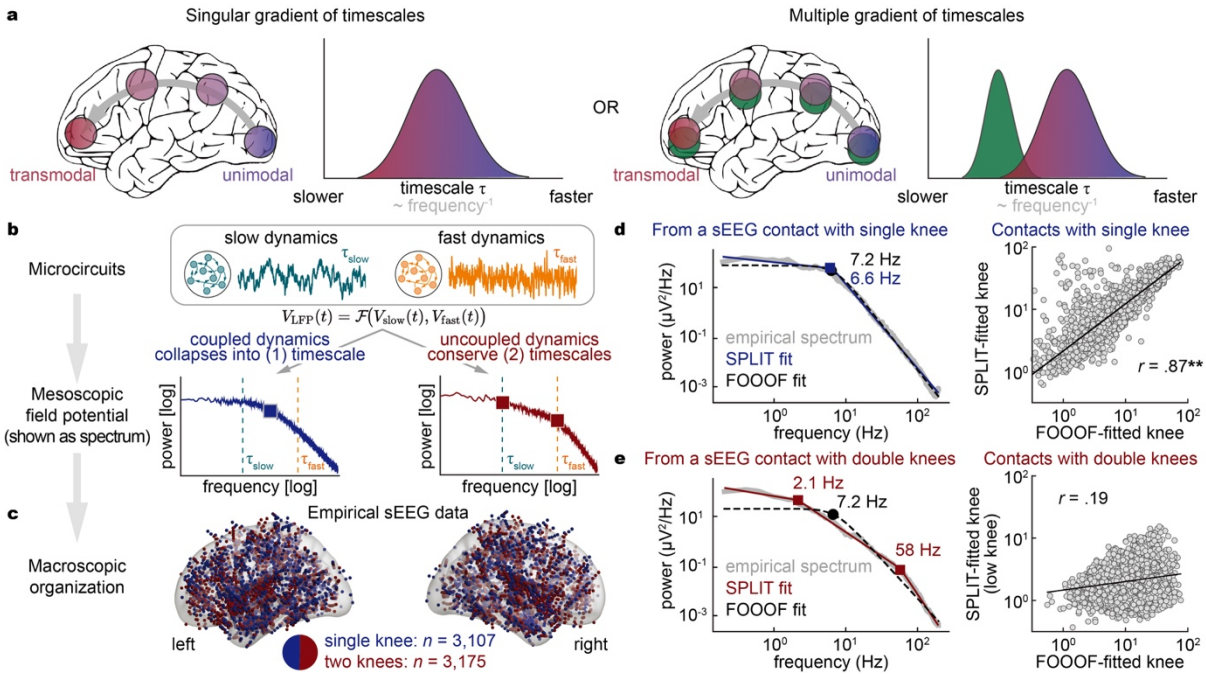

Figure 1. Hypotheses regarding the local and gradient of timescales, and estimation in large-scale human sEEG recordings reveals bipartite profiles of local timescales. **a**, Hypotheses about the gradient of timescales. Left: a dominant timescale in local regions comprises of a single gradient of timescales across brain hierarchy, increasing from unimodal to transmodal cortex. Right: multiple concurrent local timescales span into multiple gradients across brain hierarchy.

b, Demonstration of two scenarios of local timescales. Two neuronal populations with distinct intrinsic time constants (slow, fast) contribute to the local field potential (LFP). Depending on inter-population coupling, the spectrum exhibits either one knee (blue;

coupled dynamics collapsing to a single effective timescale) or two knees (red; uncoupled dynamics preserving the original dual timescales).

c, Distributions of local timescales estimated in human sEEG recordings. Brain-wide distribution of contacts best fitted by one versus two knees using SPLIT(contacts with single knee: n = 3,107; contacts with double knees: n = 3,175).

d, Consistent results of fitting simple shape spectrum are obtained by two methods with different assumptions. Left: spectral data from a representative sEEG contact fitted by FOOOF with an assumption of single knee (dashed line) and by SPLIT without imposing the number of timescales (solid line). The estimated number of knees and frequency (dot and square for FOOOF and SPLIT, respectively) are similar in two methods. Right: across contacts with single-knee, knee frequencies estimated by the two methods are correlated, demonstrating the equal efficacy of both methods in estimating local timescales from simple shape spectrum.

e, Distinct results of fitting complex shape spectrum by two methods. Left: without the assumption of number of knees, SPLIT estimated two knee frequencies. Whereas, the single-knee assumption forces FOOOF only to fit one knee frequency that is in the middle of two knee frequencies estimated by SPLIT. Right: The knee frequency estimated by FOOOF does not correlate with the values estimated by SPLIT in the contacts of complex shape spectrum (two knees estimated by SPLIT).

SPLIT reveals distribution of multiple timescales

We therefore developed a spectral analysis procedure without imposing number of timescales prior (i.e., SPLIT, see Methods for details) that inferred the properties of timescales (the number and frequency values of the spectral knees) directly from the PSD (**Fig. S2**). The method leveraged the fact that distinct timescales manifested as successive linear-like regimes in log-log PSD[8,27], with knees marking transitions between approximately linear segments[25]. Extensive validations under noisy conditions, together with sensitivity analyses for oscillation handling (**Fig. S3**) and PSD estimation (**Fig. S4**), confirmed the validity and reliability of the SPLIT fitting in estimating timescales of neural LFP dynamics.

Applying SPLIT on a large-scale human sEEG dataset, we demonstrated that single- and multi-knee spectra were both prevalent and occurred at similar rates across entire brain (**Fig. 1c**), consistent with the OU simulations that mesoscopic field potentials can express either one or multiple characteristic timescales. The prevalence of multiple timescales indicated that the assumption of single timescale and the methods built on the assumption potentially biased the fitting results and generated systematic errors. Next, we demonstrated this point by directly comparing a prevailing method (i.e., FOOOF[27]) that imposed a single-timescale assumption with the current method (i.e., SPLIT) that made no assumptions about the number of timescales.

Systematic errors in fitting knee frequency by assuming single timescale

For spectra identified as having one knee by SPLIT, the method that assumed a single-timescale and fitted by a single-Lorentzian function (FOOOF) produced highly correlated knee frequencies (n = 3,107; r = 0.87, Pearson's r correlation; **Fig. 1d**). In contrast, for two-

knee spectra, FOOOF-fitted knee values showed poor correlation with the lower-frequency knee identified by SPLIT (n = 3,175; r = 0.19; **Fig. 1e**). These results demonstrated that methods assuming a single timescale not only overlooked higher-frequency spectral knees, but, as a consequence, failed to accurately capture the dominant slow timescale. Previous studies that observed a single gradient of timescale in the brain may be biased by the single-timescale assumption. It was critical to apply the current unbiased method to investigate the brain-wide temporal architecture.

Multiple components of timescales and gradient across brain in the fast component

We examined neural timescales for each sEEG contact from an awake-state sEEG dataset (n = 136 subjects) and further analyzed the brain-wide distribution of all timescale estimates to test whether cortical temporal hierarchy was organized along a single or parallel axes **(Fig. 1a).** At the level of individual contacts, power spectra exhibited either one spectral knee (termed single knee; **Fig. 2a**) or two spectral knees (termed low- and high-knees; **Fig. 2c**) within the 0.2–200 Hz frequency range. Critically, irrespective of a contact exhibited one- or two-knee profiles, all estimated timescales segregated into two distinct cluster: a slow component (~1-10 Hz; **Fig. 2b**) and a fast component (~10-100 Hz; **Fig. 2d**). Formal model comparison confirmed that a two-component Gaussian mixture described these distributions better than single- and triple-component models (ΔBIC > 18.2, see Methods), establishing a dual-temporal architecture underlying cortical dynamics.

Crucially, these fast- and slow-component timescales related to cortical hierarchy in different manners. Projected onto two established cortical annotations, i.e., the intrinsic functional gradients[33] and the unimodal-transmodal principle gradient[34] (**Fig. 2e-f**, left), the slow component showed no systematic variation across spatial regions (all p > 0.168, one-sided Pearson's correlation, FDR corrected; **Fig. 2e-f**, middle). In contrast, the fast component exhibited a robust, monotonic gradient: the timescale decreased from sensory to association regions (all p < 0.035, one-sided Pearson's correlation, FDR corrected; **Fig. 2e-f**, right). This dissociation remained significant after accounting for inter-contact and inter-subject variance using linear mixed-effect models (fast component in both single- and double-knee spectrum: all β < -0.32, p < 0.007).

Thus, the classical functional hierarchy was selectively embedded within the fast temporal component. When we re-analyzed the same data using a standard single-Lorentzian fit (FOOOF), the relationship between timescales and cortical gradients disappeared (**Fig. S5**). The canonical hierarchy therefore emerged not from a unitary timescale gradient, but from a multi-scale architecture discernible only when fast and slow components were identified and resolved.

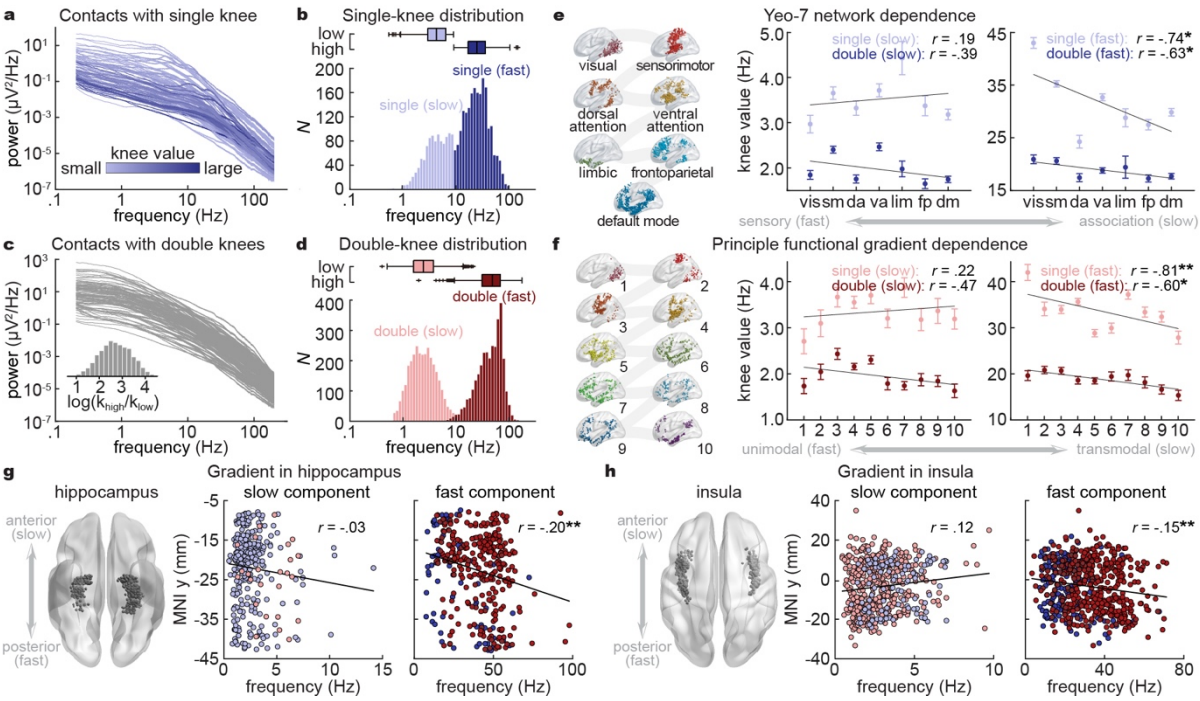

Figure 2. Two temporal components in multiple timescales and the fast component follows the gradient transition in brain-wide and regional structures.

a, PSDs from single-knee contacts. Each line represents PSD from a contact and color-coded by the frequency value of the knee.

b, Distribution of knee frequencies for single-knee spectra. A bimodal profile was revealed, separating the distribution into slow and fast components. Top, boxplots summarize each component.

c, PSDs from double-knee contacts. Each line represents PSD from a contact. Insert, the ratio between the two knees follows a lognormal distribution centered at ~2.5 (Lilliefors test, $p = 0.001$).

d, Distributions of low- and high-frequency knees for double-knee spectra. The bimodal distribution resembles similar frequency ranges observed in single-knee spectra in **b**. The slow and fast components naturally correspond to low- and high-knees, respectively.

e, Frequency values of knee frequencies as a function of spatial segmentation in the Yeo-7 functional networks. Left, the slow temporal component from both single- and double-knees spectra; Right, the fast temporal component from both single- and double-knees spectra. Only the fast temporal components correlate with the spatial gradient. Network abbreviations: vis, visual; sm, somatomotor; da, dorsal attention; va, ventral attention; lim, limbic; fp, frontoparietal; dm, default mode. In both **e** and **f**, points show mean ± s.e.m. across contacts; lines indicate linear fits; correlation coefficients show linear relations between network indices and their mean knee values.

f, Frequency values of knee frequencies as a function of spatial segmentation in the principal functional gradient (bins 1–10, ordered from unimodal/sensory to transmodal/association). Left, the slow temporal component of both single and double knees; Right, the fast temporal component of both single and double knees. Also, only the fast temporal components correlate with the spatial gradient.

g, The fast-component timescales capture the anterior-posterior gradient in the

hippocampus. Left, anatomical orientation showing anterior (slower timescale) and posterior (faster timescale) divisions of sEEG contacts. Middle, low-frequency knees do not vary with anatomical positions. Right, only fast-component knees exhibit a significant negative correlation, with anterior contacts displaying slower timescales and posterior contacts faster ones. Color codes correspond to the fast and slow temporal components in one and two knees, as in **a** and **c**.

h, The fast-component timescales also exhibit the anterior-posterior gradient in the insula. *$p < 0.05$, **$p < 0.005$.

Gradient of timescales in local brain regions

We next examined whether the gradient observed in fast-timescale at brain-wide level also miniatured in local regions. We focused on the hippocampus[10,30] and the insula[35], where prior work has identified anterior-to-posterior gradients of timescales. Consistent with our brain-wide cortical findings, only the fast-component timescales captured the gradients in both regions. In the hippocampus, fast-component timescales decreased significantly from anterior to posterior ($r = -0.21$, $p = 5\times10^{-5}$, one-sided Pearson's correlation; $\beta = -0.134$, $p = 0.001$, linear mixed-effects model; **Fig. 2g**), while slow-component timescale showed no systematic variation. An identical dissociation was observed in the insula, where the fast-component timescales similarly decreased along the anterior-posterior axis ($r = -0.15$, $p = 2\times10^{-4}$, one-sided Pearson's correlation; $\beta = -0.138$, $p = 1.2\times10^{-4}$, linear mixed-effects model; **Fig. 2h**). These results supported that the mapping principle of the gradient of timescales can be applied beyond the neocortex, and at both local and global levels, but was only appropriate in the fast temporal component of timescales.

Physiological origin of the slow-component timescales

Next, we asked if slow-component timescale that did not show functional gradient reflected potential relations with visceromotor rhythms, because the spectral knees clustered over the slow component were near heart rate (mean 1.2 Hz in the present dataset; ~1 Hz in prior work[28]) and heart rate variability can influence aperiodic spectral properties[36]. To test this hypothesis, we quantified correlations between ECG and sEEG recordings (**Fig. 3a**) and compared the ECG-sEEG correlation coefficients between contacts having low-component timescales (1-10 Hz), high-component timescales (10-100 Hz), or both (**Fig. 3b**). Contacts with slow-component timescale showed significantly stronger ECG-sEEG correlations than those without a slow-component timescale ($p = 0.0003$ for both comparisons, bootstrap, FDR corrected), whereas the presence of a fast-component timescale was not associated with stronger ECG-sEEG coupling. These results suggested that heart-related factors contributed to low-frequency neural activity that shaped slow-component timescales.

Heartbeat-locked analyses on all contacts from an example subject showed significant heart-related evoked potentials (HEPs) in a subset of contacts (red lines in **Fig. 3c**). We confirmed that the observed HEPs were not originated from direct ECG leakage and local mechanical pulsation from nearby blood vessels. No apparent ECG-like waveforms were present in the denoised sEEG components across subjects (**Fig. 3d**). Using subject-specific vascular reconstructions, HEP amplitude showed no dependence on the distance between

each sEEG contact and its nearest vessel surface (n = 474 electrodes; Pearson's r = −0.027, p = 0.55; linear mixed-effects model: β = −0.003, p = 0.10; **Fig. 3e**), arguing against a vascular pulsation artefact.

Instead, HEP were observed in all 40 subjects (**Fig. 3f**) and were broadly distributed across brain regions with enrichment in regions typically associated with the default mode and salience networks (**Fig. 3g**), consistent with a neurophysiological visceromotor interpretation[14,35]. If the gradient of timescale in the slow component was blocked by the overwhelmed HEPs, then excluding HEP-significant contacts might reveal the gradient structure. However, even after removing the contacts that showed significant HEPs, slow-component knee remained uncorrelated with cortical functional hierarchies (all p > 0.09, one-sided Pearson's correlation; all p > 0.157, linear mixed-effects model; FDR corrected; **Fig. 3h**). These results suggested that the slow-component timescale was strongly influenced by visceromotor activity, reflecting a physiological timescale but not the canonical cortical functional gradient.

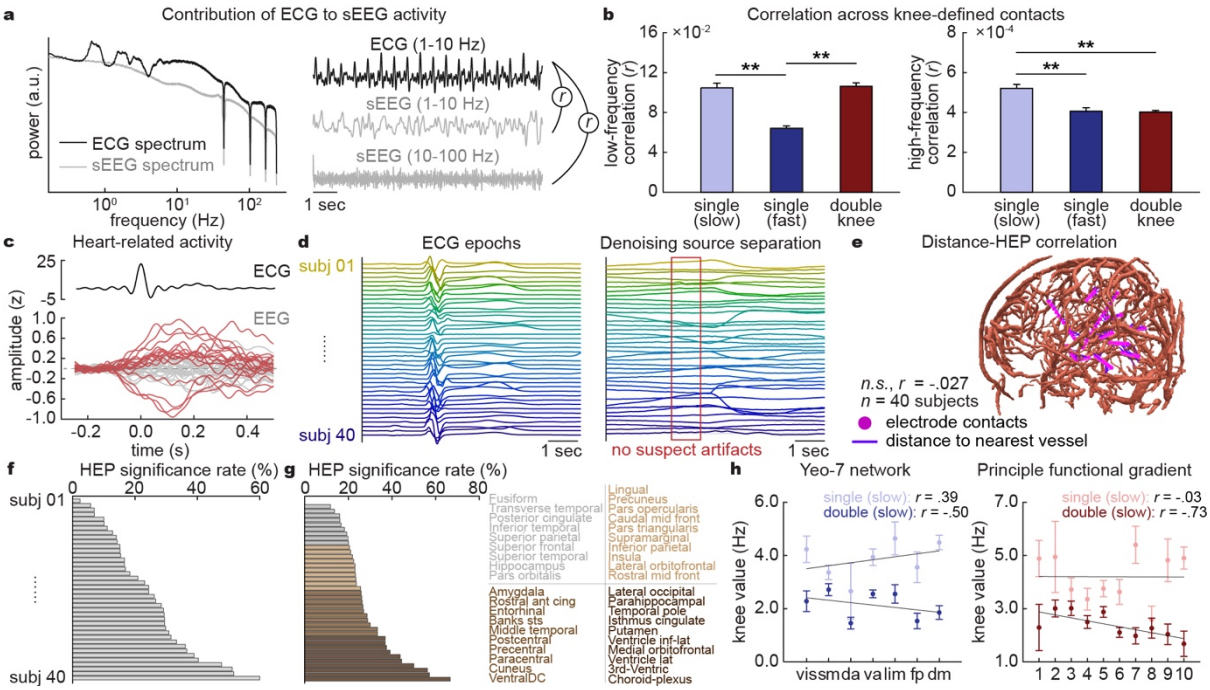

Figure 3. Cardiac-related neural activity selectively contributes to the slow-component timescales.

a, Analysis overview. Left: representative power spectra of ECG (black) and sEEG (grey) showing cardiac-related energy concentrated at low frequencies. Right: representative traces of ECG and band-limited sEEG used to quantify ECG-sEEG coupling in a low-frequency band (1-10 Hz; corresponding to low-frequency knees) and a higher-frequency band (10-100 Hz; corresponding to high-frequency knees).

b, ECG–sEEG coupling across spectral classes. Correlation strength in the low-frequency band (left) and higher-frequency band (right), with contacts grouped by spectral class (either slow- or fast-component knees from single-knee spectra, and two knees coexist in double-knee spectra). Coupling in low-frequency band is selectively elevated in contacts containing

a slow component (in both contacts of one or two knees) compared with those of only fast component. In high-frequency band, only single-knee contacts with slow component have stronger coupling with ECG. The ECG-sEEG coupling demonstrates the close relations between cardiac rhythms and the slow component. Error bars denote s.e.m. $^{**}p < 0.005$.
c, Control for ECG motor artefact using data-driven denoise source separation (DSS). Left: R-peak-aligned ECG epochs across subjects. Right: corresponding DSS components derived from sEEG that do not exhibit ECG-like waveforms (red box indicates the temporal window of original ECG features as in the left).
d, Heartbeat-related neural activity. Top: ECG waveform aligned to the R-peak. Bottom: heartbeat-evoked responses in individual contacts from a representative subject, demonstrating significant neural activity time-locked to the cardiac cycle (red traces, $^{*}p < 0.05$).
e, HEP magnitude versus vascular proximity. Three-dimensional reconstruction of intracranial electrodes (plum) overlaid on subject-specific vasculature (red). Euclidean distances were computed to the nearest vessel surface from a given contact. No significant association between HEP amplitude and electrode–vessel distance across contacts (Pearson's correlation and linear mixed-effects model), arguing against a mechanical or vascular vibration origin.
f, Subject-wise distribution of significant HEPs. Proportion of electrode contacts exhibiting significant HEPs for each subject.
g, Distribution of significant HEPs in brain regions. Anatomical summary showing heterogeneous cortical distribution of HEP-positive contacts.
h, Excluding HEP-positive contacts did not reveal gradients in the slow component. After removal of HEP-positive electrodes, slow-component timescales remain uncorrelated with cortical functional hierarchy across both functional networks, indicating that cardiac-related activity alone does not account for the absence of a functional gradient at slow component.

A consistent dual-component temporal architecture across conscious states

If the dual-component temporal architecture (i.e., slow- and fast-components timescales) is an inherent characteristic of the brain, the intrinsic property should be stable. To examine whether the timescales is invariant across levels of consciousness, we tracked spectral knees within subjects across awake, resting, sleep, and anesthetic states. In every state, the bimodal separation remained intact (model comparison, $\Delta BIC > 5.4$, see Methods; **Fig. 4a**). But both slow- and fast-component timescale were longest in the awake state and decreased in less active states (all $p < 0.012$, bootstrap, FDR corrected; **Fig. 4b**), consistent with a reduced temporal integration window[11,37].

To assess stability at the level of individual sites, we tracked whether each site's spectrum was classified as single-knee or double-knee across states. More than half of sites retained the same class during transitions (**Fig. 4c**). Class changes occurred less frequently between awake and rest than between awake and sleep or anesthesia. Thus, these results suggested that the cortex-wide segregation into fast and slow timescales was stable across the continuum of consciousness, but local spectral profile was state-dependent.

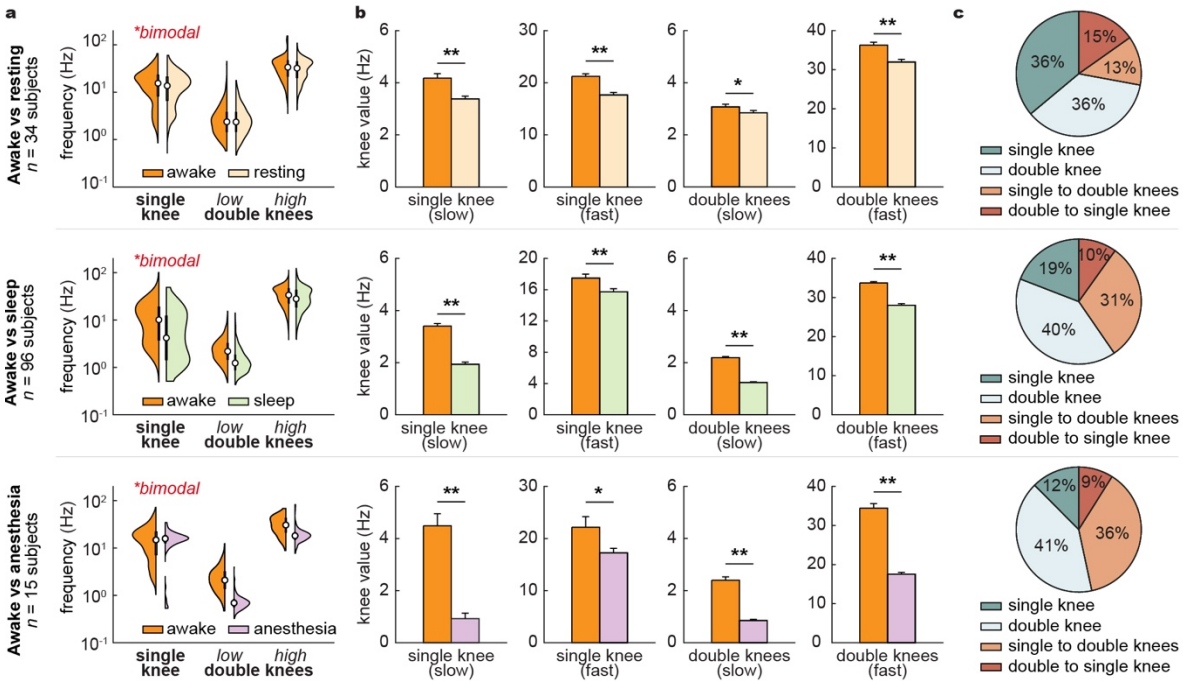

Figure 4. Consistent two-timescales organization across consciousness states

a, Distributions of knee frequencies across consciousness states. For contacts with single knee, a consistent bimodal organization of low- and high-frequency clusters was observed in all states. Another groups of contacts with double-knee were also observed with similar low- and high-frequency clusters in all states.

b, Knee values change across conscious states. Both slow- and fast-component knees are highest in the awake state and decrease progressively in less active states. Error bars denote s.e.m across electrode contacts.

c, Transitions of spectral types (i.e., contacts with single-knee or double-knee) across awake to resting, sleep, and anesthesia states. More than half of contacts preserved their original spectral class, whereas the proportion of transitions differed by state. *$p < 0.05$, **$p < 0.005$.

Discussion

Understanding the brain's diverse temporal demands is challenging due to methodological constraints and requiring high recording resolutions. By applying a novel method on large-scale human intracranial recordings, we demonstrate that the brain dynamics are built upon two dissociable temporal components. We provide clear evidence that the fast component selectively encodes the gradient of timescale, while the slow component operates independently, coupling to bodily rhythms without temporal hierarchy. This dual-component temporal architecture is intrinsic and stable across states.

Many biological systems, including neural circuits, operate across multiple interacting time scales; when these scales are sufficiently separated, the dynamics can often be decomposed into coupled fast and slow subsystems[38]. The dual-timescale structure we observe is therefore broadly consistent with established biophysical frameworks[39-41] and recent studies that report stable low- and high-frequency knees in LFP spectra[32]. Our contribution is not simply to recover fast and slow components, but to show that across cortex these components form two separable, brain-wide distributions over 0.2–200 Hz rather than a single unimodal continuum. This dissociation suggests that human temporal processing is organized around two dominant regimes with distinct functional roles. The fast component aligns with the canonical cortical hierarchy, with shorter integration in sensory regions and progressively longer integration toward association cortex, consistent with prior accounts linking the timescale gradient to sensorimotor processing and cognitive integration[11,12,37,42,43]. Notably, classical evidence for this gradient was established in spiking activity, where spike-train autocorrelation statistics vary systematically along the hierarchy[9,25], and the fast component we identify ranges at higher frequencies that are closely related to population spiking activity[44]. Therefore, separating fast and slow temporal structure is necessary to faithfully link LFP dynamics to hierarchical cortical computation.

In contrast to the fast component, the slow component remains less well understood and has been variably interpreted in current models. One influential account links slow cortical dynamic to distributed long-range recurrent connectivity, in which global coupling supports slow integration beyond local fast dynamics[45]. Moreover, recent work has argued that aperiodic neural activity can substantially reflect cardiac variability[36], and we find convergent evidence for this interpretation. In the current study, the slow component showed markedly stronger coupling to cardiac signals than the fast component (**Fig. 3b**). Indeed, the cardiac cycle can rhythmically modulate population-level neural activity, yielding measurable phase-dependent fluctuations in ongoing brain dynamics. These observations indicate that the slow component may capture not only distributed neural recurrence but also endogenous, physiology-linked dynamics that shape ongoing neural activity and has received less attention in neurophysiology and modeling. Together, these findings support a two-system view in which a slow, organism-level process integrates internal state and maintains homeostasis, thereby providing the context within which fast cortical computations operate[44,46].

This discovery was enabled by overcoming a core methodological constraint. While FOOOF

remains one of the most accessible tools for aperiodic parameterization, its core limitation lies in a prior assumption of a single Lorentzian function on the PSD (**Fig. S2**). Importantly, for non-invasive modalities such as EEG and MEG, single-knee assumption may be similarly misleading since a substantial proportion of second knees fall below 40 Hz. The current study proposes a practical pipeline for robust aperiodic feature extraction, including multiple knees and multi-slope spectral exponents, that mitigates these issues across electrophysiological modalities. Starting from pre-processed time-series data, we recommend applying IRASA to isolate oscillatory components. This method is largely parameter-free, and preserves the integrity of aperiodic component faithfully (**Fig. S2**). The cleaned signals are then transformed into power spectra using Welch's method. Note that sufficient window length is obligatory (**Fig. S4**), since short windows (e.g., 0.5-1 seconds[47-50]) are mathematically incapable of capturing slow timescales (no less than 1-2 Hz or even worse)[51-54]. Although the true knee frequency is unknown a priori, longer segments should be used to maximize the likelihood of resolving slowest timescales. Finally, the derived PSD can be fit using piecewise-linear fit or dual-Lorentzian model[25] to explicitly resolve one or more timescales and their piecewise exponents.

Lastly, our findings compel a paradigm shift: the brain's temporal organization is not a singular hierarchy, but a parallel architecture of dissociable channels. This resolves the longstanding puzzle of how rapid perception and slow visceral regulation coexist within the same neural circuitry. By transcending the oversimplified assumption of a single timescale, we establish a new analytic framework that extends from prior observations of oscillations and aperiodic exponents[26,32,49,55-57] to adopt this multi-scale lens of aperiodic and periodic neural activities.

Methods

Simulated neural signals

Generation of the simulated PSD

To evaluate the performance of the piece-wise linear fitting procedure, we generated synthetic power spectra that contained predefined changes in spectral slope (i.e., multiple bend-knee points). These spectra were designed to avoid computational bias in estimating PSD while mimicking signals with heterogeneous timescales, such that each segment of the spectrum followed a distinct linear trend on a log-log scale. The ground-truth locations of the slope changes, as well as the slope values for each segment, were explicitly controlled and therefore known for every simulated spectrum. The simulated aperiodic PSD, $L(f)$, was defined as:

$$\log_{10} P(f) = \begin{cases} a_1 - \beta_1 \log_{10} f, & f_1 \le f < f_2 \\ a_2 - \beta_2 \log_{10} f, & f_2 \le f < f_3 \\ \vdots & \\ a_K - \beta_K \log_{10} f, & f_K \le f \le f_{K+1}, \end{cases}$$

where β_k denotes the ground-truth slope for segment $K \in \{1,2,3\}$, and a_k ensures continuity at the boundaries. Vertices frequencies and slope values were parameterized explicitly, enabling direct comparison between ground truth and estimates by the algorithm.

White noise was added independently at each frequency and scaled by a multiplicative factor m, producing the final simulated spectrum:

$$P_{\text{sim}}(f) = 10^{\log_{10} P(f)} + m\,\varepsilon(f),$$

where $\varepsilon(f)$ denotes Gaussian white noise. Noise levels spanned a predefined range to evaluate robustness of the algorithm under varying signal-to-noise conditions.

All spectra were simulated over 0.2 to 200 Hz with 0.2-Hz resolution. For each condition defined by number and value of knee points and noise level, a thousand spectra were generated. For each spectrum, we quantified (i) deviation between estimated and ground-truth knee values, (ii) the accuracy of recovering the correct number of knee points, and (iii) goodness of fit.

OU process with single timescale

To generate synthetic time-series of neural signals with a single intrinsic decay timescale, we simulated a one-dimensional Ornstein-Uhlenbeck process. The process satisfies the stochastic differential equation:

$$\tau dx(t) = -x(t)dt + \sigma d\xi(t)$$

where τ is the decay constant, σ describes the strength of noise, and $\xi(t)$ is the Brownian motion process. Numerical integration was performed using the Euler-Maruyama scheme:

$$x(t + \Delta t) = (1 - 1/\tau)x(t)dt + \sigma\eta(t)\sqrt{\Delta t}$$

with a step size of Δt = 0.001 s (i.e., 1 kHz sampling rate). Produced stationary OU signals exhibiting a single exponential decay in their autocorrelation structure.

OU process with double timescales

To construct synthetic signals containing two intrinsic timescales, we simulated a two-dimensional OU system and used the sum of its two components as the final observable signal. The system dynamics are given by:

$$d\vec{x} = \mathbf{A}\vec{x}dt + \mathbf{B}d\vec{\xi}(t)$$

with a system matrix and a noise strength matrix:

$$\mathbf{A} = \begin{bmatrix} -1/\tau_1 & b/\tau_1 \\ c/\tau_2 & -1/\tau_2 \end{bmatrix}$$

$$\mathbf{B} = \begin{bmatrix} \sigma_1 & 0 \\ 0 & \sigma_2 \end{bmatrix}$$

Thus, the two coordinates evolve as coupled OU subprocesses with distinct decay constants τ_1 and τ_2,where b and c describe the strength of coupling between two components and are set to 0 when two components evlove independently. The systems were integrated using the Euler-Maruyama update:

$$\vec{x}(t + \Delta t) = \vec{x}(t) + \mathbf{A}\vec{x}dt + \mathbf{B}\vec{\xi}(t)\sqrt{dt}$$

Each simulation began from $[0,0]^T$ and ran for 15 minutes at 1 kHz. The final signal was defined as the linear sum:

$$y(t) = \vec{c}\vec{x}(t)$$

Where $\vec{c}$ is the summation vector. This yields a process whose autocorrelation is the superposition of two exponential decays with timescales τ_1 and τ_2.

OU process with oscillation(s)

To generate signals exhibiting both stochastic decay and oscillatory features, we extended the OU model by introducing a sinusoidal component to the OU signals described above. After simulating the OU system and forming the mixture signal $x_{\mathrm{OU}}(t)$, we added one or more oscillatory components of the form:

$$x_{\mathrm{osc}}(t) = A_{\mathrm{osc}} \sin(2\pi f_{\mathrm{osc}} t + \phi),$$

and final signal was constructed as:

$$x(t) = x_{\mathrm{OU}}(t) + x_{\mathrm{osc}}(t),$$

Taken together, all three kinds of OU synthetic time series combining single or double timescales, with or without oscillations, were used to evaluate the algorithm's ability to distinguish oscillatory component from aperiodic structure, and to test robustness under mixed periodic-stochastic conditions.

Empirical recordings and neural signals

Subjects

This study analyzed fully de-identified intracranial EEG data originally collected for clinical monitoring in patients with medically intractable epilepsy at the Guangdong Sanjiu Brain Hospital (Guangzhou, China) and Shenzhen Second People's Hospital (Shenzhen, China). The present research involved secondary analysis of legacy clinical data and did not require any additional data collection or patient contact. All procedures were approved by the Research Ethics Committee of the two hospitals and the Institutional Review Board of New York University Shanghai.

A total of 185 subjects (70 females; ages 18-52 years, mean age 29 years) were included. We analyzed three subsets of subjects, each providing recordings from four physiological states to enable within-subject comparisons: (i) awake dataset (136 subjects), consisting of subjects with recordings in awake state; (ii) awake-sleep dataset (96 subjects), consisting of subjects with recordings during awake and asleep; (iii) awake-resting dataset (34 subjects), consisting recordings during subjects were awake and in task-free resting state; and (iv) awake-anesthesia dataset (15 subjects), consisting of subjects with recordings during awake and general anesthesia.

Physiological Recording States

Awake state: Awake recordings were collected when patients were fully conscious and responsive during routine clinical monitoring. Patients were not given behavioral instructions and were free to engage in spontaneous everyday activities (e.g., conversation, phone use, etc). A 15-minute segment were extracted. In addition, for analyses relating the low-frequency knee to heart rate, we selected extended awake segments (30 mins to 4 hours) that contained concurrent ECG recordings.

Resting state: Resting-state recordings were obtained while patients were awake and instructed to relax without performing any task. Patients were asked to keep their eyes open or fixate on a visual point, remain still, and refrain from speaking or moving. No sensory stimulation or cognitive tasks were presented. A 5-minute resting-state segments were used for analysis.

Sleep state: Sleep recordings were acquired during natural overnight clinical monitoring. For each patient, a 15-minute segment was randomly selected from natural sleep.

Anesthesia state: Recordings when subjects were under general anesthesia were obtained during clinically indicated procedures in which anesthetic agents (e.g., propofol or sevoflurane, depending on clinical requirements) were administered by the clinical team. No task or stimulation was presented during anesthesia maintenance. A 15-minute segment was extracted for analysis.

sEEG data collection and preprocessing

Stereo-EEG was recorded with clinical depth electrodes (Sinovation, China) implanted in the brain parenchyma. Signals were amplified with a 256-channel Neuvo system and sampled at 2,000 Hz. Each electrode comprised 8-16 cylindrical contacts (0.8 mm diameter; 2 mm length; 1.5 mm inter-contact spacing). Electrode trajectories were planned with the manufacturer's ROSA software by co-registering preoperative MRI and CT. Postoperative CT acquired with electrodes in place was then co-registered to the preoperative MRI to verify implantation accuracy relative to the planned paths. The number of electrodes and placement were determined solely based on clinical purposes by the neurologists to localize epileptogenic regions as part of presurgical evaluation.

All analyses were performed in custom MATLAB scripts[58,59]. Continuous sEEG was visually screened by a neurologist (J.C.) and analyst (Y.L. and H.M.) to identify epileptiform and artifactual activity. Data were resampled to 1,000 Hz; a narrow notch (48-52, 98-102, 148-152, and 198-202 Hz) removed line noise and its harmonics. Signals were re-referenced with a local bipolar montage by differencing adjacent contacts on each shaft (the terminal contact was omitted). Contacts that were labeled as white matter or as N/A by anatomical parcellation were excluded, and outlier contacts were removed based on abnormally high mean amplitude.

Structural image and co-registration

For each patient, contact localization and anatomical labeling were performed in Brainstorm[60]. The T1 image was segmented with CAT12 and normalized to MNI152 space using SPM[61]. The postoperative CT was co-registered to the MRI with SPM12, and contacts were manually identified on the co-registered image and their coordinates were extracted in native MRI space. To obtain standardized anatomical locations, each contact's native-space coordinates were transformed into MNI152 space using the deformation fields estimated during MRI normalization. This procedure allowed an MNI coordinate for each contact for cortical-gradient analysis (see Cortical annotation).

ECG data processing

Concurrent ECG recordings were first notch filtered to remove line noise. R-peaks were detected using an automated peak-detection procedure and manually quality-checked to remove spurious detections and ectopic beats. To quantify ECG-sEEG coupling, sEEG and ECG were filtered into a low-frequency band (1-10 Hz) and a higher-frequency band (10-100 Hz), and Pearson correlations were computed between the band-limited ECG and each contact's band-limited sEEG over the continuous recordings. To assess whether ECG-sEEG coupling reflected direct ECG motor artifact contamination versus heart-related neural activity, we additionally applied a data-driven source separation (DDS) procedure to isolate components maximally coupled to ECG and inspected heartbeat-centered averages for ECG-like morphology. Heart-related neural responses were evaluated by computing HEPs, obtained by averaging sEEG epochs time-locked to the ECG R-peak (baseline-corrected to the pre-R interval). Electrodes were labeled as HEP-significant using a two-sided bootstrap test across -200-0 ms baseline and 0-200 ms activity.

MR angiography

All vascular analyses began with raw magnetic resonance angiography (MRA) images. Vessel enhancement and segmentation were performed in 3D Slicer using a vesselness-based filter to improve contrast of tubular vascular structures against background tissue. Subject-specific vascular masks were generated and were co-registered in SPM to each participant's T1-weighted anatomical image using a rigid-body transformation, ensuring spatial alignment across vascular, anatomical, and electrode coordinate spaces. Finally, three-dimensional surface models of the vasculature were reconstructed from the aligned masks via the marching cubes algorithm. Vertex coordinates of each model were converted into world coordinates using the appropriate affine transform, enabling consistent distance

measurements between electrode locations and nearby vascular structures.

Pipeline of timescale estimate

Fitting algorithms

SPLIT fitting (spectral piecewise-linear inference of timescale): To identify multiple neural timescales in the aperiodic spectrum, we modeled PSD in log-log space, where 1/f-like spectra become approximately piecewise linear. The PSD estimate parameter and oscillation removal method were chosen to capture multiple spectral knees (**Table 1**). In this domain, each linear segment corresponds to a distinct power-law regime, and the transitions between segments, i.e., the spectral knees, defined characteristic timescales. Because the frequency sampling is highly non-uniform in log space, with dense sampling at high frequencies and sparse sampling at low frequencies, direct fitting would overweight the high-frequency range. To ensure equal contribution across frequencies, the log-transformed PSD was linearly interpolated onto an evenly spaced grid of 1,000 log-frequency points spanning the full fitting range (0.2-200 Hz). This procedure preserves the 1/f curvature while standardizing sampling density for segmentation.

For each contact, we fitted a piecewise linear model with K segments ($K = 1, \dots, 3$):

$$y(x) = \begin{cases} a_1 x + b_1, & x_1 \le x < c_1 \\ a_2 x + b_2, & c_1 \le x < c_2 \\ & \vdots \\ a_K x + b_K, & c_{K-1} \le x \le x_K, \end{cases}$$

where a_k were local slopes and c_j were internal breakpoints. The negative slopes ($\beta_k = -a_k$) represented local aperiodic exponents, while breakpoints defined knee frequencies $f_{\text{knee}} = 10^{c_j}$.

To avoid enforcing a predetermined number of knees, we selected the optimal number of segments K by minimizing a penalized objective that traded off goodness-of-fit and model complexity. The regularization weight λ was chosen through systematic qualitative assessment that best preserved true curvature without over-segmentation. This fixed λ was then applied uniformly across all contacts. For each candidate $K = 1, \dots, 3$, the penalized loss was estimated using Bayesian optimization, and the model was refit using the optimal K^*. Internal breakpoints were extracted as knee frequencies, and corresponding slopes. This procedure estimated, in every contact, the number of knees, their frequencies in Hz, and the associated spectral exponents, forming the basis for all subsequent timescale analyses.

Autocorrelation fitting: Autocorrelation-based timescale estimates were obtained by fitting exponential decay models to the broadband ACF of each sEEG electrode contact. Continuous data were segmented into overlapping windows (50% overlap), with window lengths chosen to capture slow dynamics (**Table 1**). Within each window, the ACF was computed using FFT-based estimation up to the maximum lag, and windowed ACFs were averaged to yield a stable mean ACF. The fitting range was restricted to the portion of the ACF above 0 of its maximum to avoid contamination from long-lag noise. For empirical data, we fitted a shifted exponential of the form

$$R(t) \approx A\left(e^{-t/\tau} + B\right),$$

where τ is the autocorrelation timescale and B captures residual slow drifts. Parameters were estimated via differential evolution using broad bounds, and non-convergent fits were excluded. For simulated signals containing two ground-truth timescales, we additionally fitted a bi-exponential model,

$$R(t) \approx A_1 e^{-t/\tau_1} + (1 - A_1) e^{-t/\tau_2} + B,$$

with $A_1 \in (0,1)$ enforcing a convex mixture of two components. This dual-exponential model was used solely to validate the behavior of ACF estimators under multiscale dynamics and was not applied to human data.

FOOOF fitting: For comparison with models with single-knee assumption, we fit each power spectrum using the FOOOF algorithm[27], which parameterizes the aperiodic component using a Lorentzian 1/f function and Gaussian peaks. FOOOF was applied across simulations and empirical data analysis using the following parameters: knee mode, a maximum of three oscillatory peaks (max_n_peaks = 3), peak width limits of 1-12 Hz (peak_width_limits=[1, 12]), a minimum peak height of 0.2 (min_peak_height = 0.2), and a peak-detection threshold of 2 (peak_threshold = 2). All spectra were fit over the 0.2-200 Hz frequency range.

Oscillatory activity removal

Oscillatory components were removed using the Irregular-Resampling Auto-Spectral Analysis procedure[62], which separated the broadband aperiodic spectrum from narrowband rhythmic peaks through non-integer resampling. For each sEEG electrode contact, continuous data were divided into 70-s windows (**Table 1**), and the signal was resampled using a set of multiplicative factors h and 1/h (e.g., $h = 1.1, 1.2, \ldots$), stretching and compressing oscillatory components while leaving the fractal 1/f background unchanged. Averaging the spectra across all resampling factors canceled out the oscillatory components, yielding a fractal (aperiodic) spectrum; subtracting this from the original power spectrum produces an estimate of the oscillatory residual. IRASA was applied over 0.01-400 Hz (due to algorithmic requirement) using the same sampling rate and windowing parameters as the PSD computation, and the fractal spectrum was taken forward for knee fitting.

FOOOF-based oscillation removal was also used only for comparison, using the above-mentioned parameters. The aperiodic component estimated by FOOOF was subtracted from the original PSD to obtain a second oscillation-removed spectrum used solely for cross-method validation.

Table 1. Summary of datasets and analysis configurations

Data	Window length	Oscillation removal method	Fitting methods	Relevant figures
Awake data (*n* = 136)	70s, 50% overlap	FOOOF	FOOOF	**Fig. 2d-e**
	70s, 50% overlap	FOOOF	SPLIT	**Fig. 2c, d-e**

Awake data (*n* = 136)	70s, 50% overlap	IRASA	SPLIT	**Fig. 3**
Awake and resting-state data (*n* = 34)				**Fig. 4**, first row
Awake and asleep data (*n* = 96)				**Fig. 4**, second row
Awake and anesthesia data (*n* = 15)				**Fig. 4**, third row
OU simulations with neuronal subsystems	70s, 50% overlap	IRASA	SPLIT	**Fig. S1**
PSD simulations	-	-	SPLIT	**Fig. S2b**
OU simulation with oscillations	5s, 50% overlap	FOOOF	SPLIT	**Fig. S3**
	5s, 50% overlap	IRASA	SPLIT	**Fig. S3**
OU simulation with multiple timescale(s)	1-100s, 50% overlap	-	SPLIT	**Fig. S4a, c**
	1-100s, 50% overlap	-	Autocorrelation	**Fig. S4b, d**
Awake data (*n* = 136)		FOOOF	FOOOF	**Fig. S5**

Cortical annotation

To place local timescale estimates within established macroscale organization, we examined their distribution across two widely used cortical atlases: the seven intrinsic functional networks[33], and the principal unimodal-transmodal functional gradient[10]. For each atlas, contacts belonging to the same gradient bin were grouped, and low- and high-frequency knees were averaged separately within each group. These complementary annotations capture distinct aspects of cortical hierarchy and provide a principled framework for assessing large-scale organization of timescales.

Statistical analysis

All statistical comparisons were conducted within subjects, and false discovery rate (FDR) correction was applied to control for multiple comparisons.

Bootstrap test

Bias-corrected and accelerated bootstrapping[63] was used to compare difference between conditions (**Fig. 3b** and **Fig. 4b**). In the bootstrap procedure, participants were resampled 10,000 times with replacement. For each comparison, we calculated the proportion A of

bootstrap samples in which the mean knee value in one condition was greater (or smaller) than in the other condition. All tests were two-sided, with formular to obtain p-value: $p = (2 \cdot \min(A, 1 - A) \cdot 10{,}000 + 1)/10{,}001$.

Bimodal distribution test

To assess whether the data exhibited a unimodal or bimodal distribution, we adopted a model-based approach using Gaussian mixture models. The data were first log-transformed, after which Gaussian mixture models with one to four components were fitted using the expectation-maximization algorithm. To ensure robust parameter estimation, each model was fitted with multiple random initializations, and covariance regularization was applied to avoid numerical instability. Model selection was performed using the Bayesian Information Criterion, which balances goodness of fit against model complexity. If the model with two components yielded the lowest BIC, indicating that a bimodal distribution provided the most parsimonious explanation of the data.

Correlation analysis

Pearson's correlation was used to quantify associations between spectral knee frequency and the cortical functional gradient (**Fig. 2e-f** and **Fig. 3h**), between knees estimated using FOOOF and SPLIT fitting (**Fig. 1d-e**), between contact-vessel distance and HEP amplitude (Fig. 3e), and between sEEG and ECG time series (**Fig. 3a**).

Linear mixed effect model

To complement correlation analyses and account for repeated measurements across channels and subjects, we further performed linear mixed-effects (LME) modeling. Functional gradient was entered as a fixed effect, while subject- and channel-level variability were modeled as random intercepts, with channels nested within subjects. For the relation between knee and gradient, we used equation: $\mathrm{knee} \sim \mathrm{gradient} + (1 \mid \mathrm{subject{:}\,channel})$; for the relation between HEP amplitude and Euclidean distance to vessel, we used equation: $\mathrm{HEP} \sim \mathrm{distance} + (1 \mid \mathrm{subject{:}\,channel})$. Models were fitted using MATLAB's fitlme function.

Data availability

The de-identified sEEG datasets supporting the findings of this study are available at http://github.com/. Readers interested in accessing the raw dataset may contact the lead author. Data access will be granted to named individuals in accordance with ethical guidelines for the reuse of clinical data, subject to the completion of a formal data-sharing agreement and institutional approval.

Code availability

The analysis codes supporting the findings of the study are available at our GitHub repository: https://github.com/. The SPLIT algorithm code is openly available in both MATLAB and python versions with supporting documents at https://slang.science/.

Acknowledgement

We sincerely thank Yiduo Lu, Youcun Zheng, Ruoyu Wu, Mingxuan Fang, Xiaofeng Zeng,

Yuling Huang, and Peiyu He for assisting in data preparation. This study is supported by the National Natural Science Foundation of China 32271101 (X.T.), the Brain Science and Brain-like Intelligence Technology - National Science and Technology Major Project No. 2022ZD0204600 and the Natural Science Foundation of China Grant No. 31771147 (Z.L. and L.T.), and Program of AI-Driven Initiative to Promote Research Paradigm Reform and Empower Disciplinary Advancement by Shanghai Municipal Education Commission (SMEC), Program of Introducing Talents of Discipline to Universities, Base B16018, and NYU Shanghai Boost Fund to X.T.

Author contributions

All authors initiated and designed the study. Y.L. and H.M. conceived of and coded the algorithm. Y.L., H.M., Z.L., and Q.L. contributed code and tested the algorithm against real and simulated data. J.C. and Y.C. collected data. Y.L. and H.M. analyzed data. L.T, Z.X. and X.T. provided overall supervision and guidance throughout the project. All authors contributed to the manuscript.

Declaration of interests

The authors declare no competing financial interests.

References

1 Theriault, J. E. *et al.* It's not the thought that counts: Allostasis at the core of brain function. *Neuron* **113**, 4107-4133 (2025). https://doi.org:10.1016/j.neuron.2025.09.028

2 Honey, C. J. *et al.* Slow cortical dynamics and the accumulation of information over long timescales. *Neuron* **76**, 423-434 (2012). https://doi.org:10.1016/j.neuron.2012.08.011

3 Hasson, U., Yang, E., Vallines, I., Heeger, D. J. & Rubin, N. A hierarchy of temporal receptive windows in human cortex. *J Neurosci* **28**, 2539-2550 (2008). https://doi.org:10.1523/JNEUROSCI.5487-07.2008

4 Giraud, A. L. & Poeppel, D. Cortical oscillations and speech processing: emerging computational principles and operations. *Nat Neurosci* **15**, 511-517 (2012). https://doi.org:10.1038/nn.3063

5 Miller, J. A. & Constantinidis, C. Timescales of learning in prefrontal cortex. *Nat Rev Neurosci* **25**, 597-610 (2024). https://doi.org:10.1038/s41583-024-00836-8

6 Pritchard, W. S. The brain in fractal time: 1/f-like power spectrum scaling of the human electroencephalogram. *Int J Neurosci* **66**, 119-129 (1992). https://doi.org:10.3109/00207459208999796

7 Hausdorff, J. M. & Peng, C. Multiscaled randomness: A possible source of 1/f noise in biology. *Phys Rev E Stat Phys Plasmas Fluids Relat Interdiscip Topics* **54**, 2154-2157 (1996). https://doi.org:10.1103/physreve.54.2154

8 He, B. J. Scale-free brain activity: past, present, and future. *Trends Cogn Sci* **18**, 480-487 (2014). https://doi.org:10.1016/j.tics.2014.04.003

9 Murray, J. D. *et al.* A hierarchy of intrinsic timescales across primate cortex. *Nat Neurosci* **17**, 1661-1663 (2014). https://doi.org:10.1038/nn.3862

10 Raut, R. V., Snyder, A. Z. & Raichle, M. E. Hierarchical dynamics as a macroscopic organizing principle of the human brain. *Proc Natl Acad Sci U S A* **117**, 20890-20897 (2020). https://doi.org:10.1073/pnas.2003383117

11 Wolff, A. *et al.* Intrinsic neural timescales: temporal integration and segregation. *Trends Cogn Sci* **26**, 159-173 (2022). https://doi.org:10.1016/j.tics.2021.11.007

12 Soltani, A., Murray, J. D., Seo, H. & Lee, D. Timescales of Cognition in the Brain. *Curr Opin Behav Sci* **41**, 30-37 (2021). https://doi.org:10.1016/j.cobeha.2021.03.003

13 Kleckner, I. R. *et al.* Evidence for a Large-Scale Brain System Supporting Allostasis and Interoception in Humans. *Nat Hum Behav* **1**, 0069 (2017). https://doi.org:10.1038/s41562-017-0069

14 Zhang, J. *et al.* Cortical and subcortical mapping of the human allostatic–interoceptive system using 7 Tesla fMRI. *Nature Neuroscience*, 1-12 (2025).

15 Buzsáki, G. *Rhythms of the Brain*. (Oxford university press, 2006).

16 Stanyard, R. A. *et al.* Aperiodic and Hurst EEG exponents across early human brain development: A systematic review. *Dev Cogn Neurosci* **68**, 101402 (2024). https://doi.org:10.1016/j.dcn.2024.101402

17 Donoghue, T. A Systematic Review of Aperiodic Neural Activity in Clinical Investigations. *Eur J Neurosci* **62**, e70255 (2025). https://doi.org:10.1111/ejn.70255

18 Pani, S. M., Saba, L. & Fraschini, M. Clinical applications of EEG power spectra aperiodic component analysis: A mini-review. *Clin Neurophysiol* **143**, 1-13 (2022). https://doi.org:10.1016/j.clinph.2022.08.010

19 Wu, K. & Gollo, L. L. Mapping and modeling age-related changes in intrinsic neural timescales. *Commun Biol* **8**, 167 (2025). https://doi.org:10.1038/s42003-025-07517-x

20 Golesorkhi, M., Gomez-Pilar, J., Tumati, S., Fraser, M. & Northoff, G. Temporal hierarchy of intrinsic neural timescales converges with spatial core-periphery organization. *Commun Biol* **4**, 277 (2021). https://doi.org:10.1038/s42003-021-01785-z

21 Cavanagh, S. E., Wallis, J. D., Kennerley, S. W. & Hunt, L. T. Autocorrelation structure at rest predicts value correlates of single neurons during reward-guided choice. *Elife* **5**, e18937 (2016). https://doi.org:10.7554/eLife.18937

22 Siegle, J. H. *et al.* Survey of spiking in the mouse visual system reveals functional hierarchy. *Nature* **592**, 86-92 (2021). https://doi.org:10.1038/s41586-020-03171-x

23 Wilting, J. & Priesemann, V. Inferring collective dynamical states from widely unobserved systems. *Nat Commun* **9**, 2325 (2018). https://doi.org:10.1038/s41467-018-04725-4

24 Li, G., Li, S. & Wang, X. J. A hierarchy of time constants and reliable signal propagation in the marmoset cerebral cortex. *Nat Commun* **16**, 11640 (2025). https://doi.org:10.1038/s41467-025-66699-4

25 Gao, R., van den Brink, R. L., Pfeffer, T. & Voytek, B. Neuronal timescales are functionally dynamic and shaped by cortical microarchitecture. *Elife* **9**, e61277 (2020). https://doi.org:10.7554/eLife.61277

26 Wilson, L. E., da Silva Castanheira, J. & Baillet, S. Time-resolved parameterization of aperiodic and periodic brain activity. *Elife* **11**, e77348 (2022). https://doi.org:10.7554/eLife.77348

27 Donoghue, T. *et al.* Parameterizing neural power spectra into periodic and aperiodic components. *Nat Neurosci* **23**, 1655-1665 (2020). https://doi.org:10.1038/s41593-020-00744-x

28 He, B. J., Zempel, J. M., Snyder, A. Z. & Raichle, M. E. The temporal structures and functional significance of scale-free brain activity. *Neuron* **66**, 353-369 (2010). https://doi.org:10.1016/j.neuron.2010.04.020

29 Miller, K. J., Sorensen, L. B., Ojemann, J. G. & den Nijs, M. Power-law scaling in the brain surface

electric potential. *PLoS Comput Biol* **5**, e1000609 (2009). https://doi.org:10.1371/journal.pcbi.1000609

30 Rait, L. I., Wanjia, G., Ye, Z., DuBrow, S. & Kuhl, B. A. Hippocampal Drift Rate Reflects the Temporal Organization of Memories. *J Neurosci* **45**, e0909252025 (2025). https://doi.org:10.1523/JNEUROSCI.0909-25.2025

31 Freeman, W. J. & Zhai, J. Simulated power spectral density (PSD) of background electrocorticogram (ECoG). *Cogn Neurodyn* **3**, 97-103 (2009). https://doi.org:10.1007/s11571-008-9064-y

32 Lendner, J. D., Lin, J. J., Larsson, P. G. & Helfrich, R. F. Multiple Intrinsic Timescales Govern Distinct Brain States in Human Sleep. *J Neurosci* **44**, e0171242024 (2024). https://doi.org:10.1523/JNEUROSCI.0171-24.2024

33 Schaefer, A. *et al.* Local-Global Parcellation of the Human Cerebral Cortex from Intrinsic Functional Connectivity MRI. *Cereb Cortex* **28**, 3095-3114 (2018). https://doi.org:10.1093/cercor/bhx179

34 Margulies, D. S. *et al.* Situating the default-mode network along a principal gradient of macroscale cortical organization. *Proc Natl Acad Sci U S A* **113**, 12574-12579 (2016). https://doi.org:10.1073/pnas.1608282113

35 Livneh, Y. & Andermann, M. L. Cellular activity in insular cortex across seconds to hours: Sensations and predictions of bodily states. *Neuron* **109**, 3576-3593 (2021). https://doi.org:10.1016/j.neuron.2021.08.036

36 Schmidt, F. *et al.* Age-related changes in 'cortical' 1/f dynamics are linked to cardiac activity. *Elife* **13**, RP100605 (2025). https://doi.org:10.7554/eLife.100605

37 Senkowski, D. & Engel, A. K. Multi-timescale neural dynamics for multisensory integration. *Nat Rev Neurosci* **25**, 625-642 (2024). https://doi.org:10.1038/s41583-024-00845-7

38 Bertram, R. & Rubin, J. E. Multi-timescale systems and fast-slow analysis. *Math Biosci* **287**, 105-121 (2017). https://doi.org:10.1016/j.mbs.2016.07.003

39 Marom, S. & Marder, E. A biophysical perspective on the resilience of neuronal excitability across timescales. *Nat Rev Neurosci* **24**, 640-652 (2023). https://doi.org:10.1038/s41583-023-00730-9

40 Gjorgjieva, J., Drion, G. & Marder, E. Computational implications of biophysical diversity and multiple timescales in neurons and synapses for circuit performance. *Curr Opin Neurobiol* **37**, 44-52 (2016). https://doi.org:10.1016/j.conb.2015.12.008

41 Coombes, S. Large-scale neural dynamics: simple and complex. *Neuroimage* **52**, 731-739 (2010). https://doi.org:10.1016/j.neuroimage.2010.01.045

42 Wang, X. J. Macroscopic gradients of synaptic excitation and inhibition in the neocortex. *Nat Rev Neurosci* **21**, 169-178 (2020). https://doi.org:10.1038/s41583-020-0262-x

43 Golesorkhi, M. *et al.* The brain and its time: intrinsic neural timescales are key for input processing. *Commun Biol* **4**, 970 (2021). https://doi.org:10.1038/s42003-021-02483-6

44 Buzsaki, G. Large-scale recording of neuronal ensembles. *Nat Neurosci* **7**, 446-451 (2004). https://doi.org:10.1038/nn1233

45 Chaudhuri, R., He, B. J. & Wang, X. J. Random Recurrent Networks Near Criticality Capture the Broadband Power Distribution of Human ECoG Dynamics. *Cereb Cortex* **28**, 3610-3622 (2018). https://doi.org:10.1093/cercor/bhx233

46 Foster, B. L. *et al.* Spontaneous neural dynamics and multi-scale network organization. *Frontiers in systems neuroscience* **10**, 7 (2016).

47 Cusinato, R. *et al.* Intrinsic Neural Timescales in the Temporal Lobe Support an Auditory Processing Hierarchy. *J Neurosci* **43**, 3696-3707 (2023). https://doi.org:10.1523/JNEUROSCI.1941-22.2023

48 Cusinato, R., Seiler, A., Schindler, K. & Tzovara, A. Sleep Modulates Neural Timescales and Spatiotemporal Integration in the Human Cortex. *J Neurosci* **45** (2025). https://doi.org:10.1523/JNEUROSCI.1845-24.2025

49 Bush, A., Zou, J. F., Lipski, W. J., Kokkinos, V. & Richardson, R. M. Aperiodic components of local field potentials reflect inherent differences between cortical and subcortical activity. *Cereb Cortex* **34** (2024). https://doi.org:10.1093/cercor/bhae186

50 Raposo, I. *et al.* Human attention-guided visual perception is governed by rhythmic oscillations and aperiodic timescales. *PLoS Biol* **23**, e3003232 (2025). https://doi.org:10.1371/journal.pbio.3003232

51 Zeraati, R., Engel, T. A. & Levina, A. A flexible Bayesian framework for unbiased estimation of timescales. *Nat Comput Sci* **2**, 193-204 (2022). https://doi.org:10.1038/s43588-022-00214-3

52 Afyouni, S., Smith, S. M. & Nichols, T. E. Effective degrees of freedom of the Pearson's correlation coefficient under autocorrelation. *Neuroimage* **199**, 609-625 (2019). https://doi.org:10.1016/j.neuroimage.2019.05.011

53 Bartlett, M. S. On the Theoretical Specification and Sampling Properties of Autocorrelated Time-Series. *J Roy Stat Soc B* **8**, 27-41 (1946).

54 Marom, S. Neural timescales or lack thereof. *Prog Neurobiol* **90**, 16-28 (2010). https://doi.org:10.1016/j.pneurobio.2009.10.003

55 Brake, N. *et al.* A neurophysiological basis for aperiodic EEG and the background spectral trend. *Nat Commun* **15**, 1514 (2024). https://doi.org:10.1038/s41467-024-45922-8

56 Donoghue, T., Schaworonkow, N. & Voytek, B. Methodological considerations for studying neural oscillations. *Eur J Neurosci* **55**, 3502-3527 (2022). https://doi.org:10.1111/ejn.15361

57 Gerster, M. *et al.* Separating Neural Oscillations from Aperiodic 1/f Activity: Challenges and Recommendations. *Neuroinformatics* **20**, 991-1012 (2022). https://doi.org:10.1007/s12021-022-09581-8

58 Lu, Y., Jin, P., Ding, N. & Tian, X. Delta-band neural tracking primarily reflects rule-based chunking instead of semantic relatedness between words. *Cereb Cortex* **33**, 4448-4458 (2023). https://doi.org:10.1093/cercor/bhac354

59 Lu, Y., Jin, P., Pan, X. & Ding, N. Delta-band neural activity primarily tracks sentences instead of semantic properties of words. *Neuroimage* **251**, 118979 (2022). https://doi.org:10.1016/j.neuroimage.2022.118979

60 Tadel, F., Baillet, S., Mosher, J. C., Pantazis, D. & Leahy, R. M. Brainstorm: a user-friendly application for MEG/EEG analysis. *Comput Intell Neurosci* **2011**, 879716 (2011). https://doi.org:10.1155/2011/879716

61 Tzourio-Mazoyer, N. *et al.* Automated anatomical labeling of activations in SPM using a macroscopic anatomical parcellation of the MNI MRI single-subject brain. *Neuroimage* **15**, 273-289 (2002). https://doi.org:10.1006/nimg.2001.0978

62 Wen, H. & Liu, Z. Separating Fractal and Oscillatory Components in the Power Spectrum of Neurophysiological Signal. *Brain Topogr* **29**, 13-26 (2016). https://doi.org:10.1007/s10548-015-0448-0

63 Efron, B. & Tibshirani, R. J. *An Introduction to the Bootstrap*. (CRC press, 1994).